



Anisotropic diffusion creep in postperovskite provides a new model for deformation at the core–mantle boundary

David P. Dobson^{a,b,1}, Alexander Lindsay-Scott^a, Simon A. Hunt^a, Edward Bailey^{a,2}, Ian G. Wood^a, John P. Brodholt^{a,c}, Lidunka Vocollo^a, and John Wheeler^d

^aDepartment of Earth Sciences, University College London, WC1E 6BT London, United Kingdom; ^bBayerisches Geoinstitut, Universität Bayreuth, D-95440 Bayreuth, Germany; ^cCentre for Earth Evolution and Dynamics, University of Oslo, 0316 Oslo, Norway; and ^dDepartment of Earth, Ocean and Ecological Sciences, University of Liverpool, Liverpool L69 3GP, United Kingdom

Edited by Bruce Watson, Rensselaer Polytechnic Institute, Troy, NY, and approved November 13, 2019 (received for review August 26, 2019)

The lowermost portion of Earth's mantle (D'') above the core–mantle boundary shows anomalous seismic features, such as strong seismic anisotropy, related to the properties of the main mineral MgSiO₃ postperovskite. But, after over a decade of investigations, the seismic observations still cannot be explained simply by flow models which assume dislocation creep in postperovskite. We have investigated the chemical diffusivity of perovskite and postperovskite phases by experiment and ab initio simulation, and derive equations for the observed anisotropic diffusion creep. There is excellent agreement between experiments and simulations for both phases in all of the chemical systems studied. Single-crystal diffusivity in postperovskite displays at least 3 orders of magnitude of anisotropy by experiment and simulation ($D_a = 1,000 D_b$; $D_b \approx D_c$) in zinc fluoride, and an even more extreme anisotropy is predicted ($D_a = 10,000 D_c$; $D_c = 10,000 D_b$) in the natural MgSiO₃ system. Anisotropic chemical diffusivity results in anisotropic diffusion creep, texture generation, and a strain-weakening rheology. The results for MgSiO₃ postperovskite strongly imply that regions within the D'' region of Earth dominated by postperovskite will 1) be substantially weaker than regions dominated by perovskite and 2) develop a strain-induced crystallographic-preferred orientation with strain-weakening rheology. This leads to strain localization and the possibility to bring regions with significantly varying textures into close proximity by strain on narrow shear zones. Anisotropic diffusion creep therefore provides an attractive alternative explanation for the complexity in observed seismic anisotropy and the rapid lateral changes in seismic velocities in D''.

postperovskite | D'' | diffusion creep | anisotropy

The postperovskite phase (CaIrO₃-type) of (Mg,Fe)(Si,Al)O₃ is stable at pressures above ~120 GPa (1–3), corresponding to the D'' region of Earth's lowermost mantle. Its strongly anisotropic elastic and rheological properties have been invoked to explain observations of strong seismic anisotropy in D'' which are interpreted as requiring creep by a dislocation migration process. If we can determine the active flow mechanisms of postperovskite, this then offers the possibility of interpreting the D'' seismic anisotropy in terms of convective patterns deep in Earth, and using them to map flow farther back into deep time than current plate reconstructions allow (4–7). This has important implications for understanding many first-order questions about the deep Earth, such as the degree of mixing, the ultimate fate of slabs, and the longevity of seismic anomalies such as the large low-shear-velocity provinces (LLSVPs).

In order to interpret the seismic observations, one must fully understand the relationships between strain and texture generation in mantle rocks. Although there have been many studies attempting to do this for postperovskite (5, 8–15), no unique solution has been found which fits the globally observed seismic anisotropy using a single slip system in postperovskite (e.g., ref. 14). In particular, strong changes in anisotropy observed around

hot regions of D'' are difficult to explain by simple flow and dislocation creep. One aspect that has been relatively ignored is the remarkably large anisotropy in diffusion rates along different crystallographic directions predicted in ab initio calculations, with up to 8 orders of magnitude difference between the fast and slow diffusion directions in postperovskite (16). This would be the largest diffusion anisotropy seen in any material, to the best of our knowledge, and, if correct, might have significant implications for the dynamics of the core–mantle boundary region. However, there have not, as yet, been any studies to test whether the predicted diffusion anisotropy is real. Furthermore, only one study has investigated the effect of the anisotropic diffusion on the rheology of D'' (17) and only for deformation by either pure dislocation glide or climb-assisted glide. And crucially, there have been no studies, to date, of the effect of extreme anisotropic diffusion on lattice diffusion creep. This is because the observation of seismic anisotropy is generally thought to require dislocation creep. However, the high temperatures and low stresses of the core–mantle boundary, combined with the very small grain size expected in postperovskite (11, 18), would argue for diffusion creep to be the active deformation mechanism in D''. Here we present a combined ab initio simulation and multianvil experimental study of chemical diffusion in both the perovskite and postperovskite structures in a fluoride analog system. Fluorides have been shown to be a good analog for the silicate system with similar crystal chemistry in both perovskite and postperovskite

Significance

Earth's core–mantle region is an important, but poorly understood, region which drives mantle convection (and hence surface processes) by heat transfer from the core to the mantle. Seismic observations show the complexity of the region, but current geodynamic modeling of lowermost mantle flow is hindered by an incomplete understanding of the rheology of the main mineral, postperovskite. Here we show that postperovskite is strongly anisotropic in diffusion creep and hence will show nonlinear behaviors during deformation, including strain weakening and localization. This will help to explain much of the observed seismic complexity of the core–mantle boundary region.

Author contributions: D.P.D. designed research; D.P.D., A.L.-S., S.A.H., and E.B. performed research; D.P.D., A.L.-S., I.G.W., L.V., and J.W. analyzed data; and D.P.D., I.G.W., J.P.B., and J.W. wrote the paper.

The authors declare no competing interest.

This article is a PNAS Direct Submission.

Published under the PNAS license.

¹To whom correspondence may be addressed. Email: d.dobson@ucl.ac.uk.

²Present address: Department of Chemical Engineering, Imperial College London, London SW7 2AZ, United Kingdom.

This article contains supporting information online at <https://www.pnas.org/lookup/suppl/doi:10.1073/pnas.1914826116/-DCSupplemental>.

First published December 11, 2019.

structures (ref. 19 and references therein) and transforming via the same martensitic-like mechanism between the 2 phases (11). We find that, similar to the silicate system, the fluoride system also displays extreme anisotropy in chemical diffusivity in the postperovskite phase. By developing an analytical solution for strain in grains with anisotropic chemical diffusivities, we show that diffusion anisotropy will create a strain-weakening rheology, with the ultimate strain rate controlled by the fastest diffusion direction. We observe that the crystallographically controlled shape anisotropy of crystals deforming in lattice diffusion creep leads to crystallographic-preferred orientation in crystals deforming by lattice diffusion creep, and we discuss the implications of anisotropic diffusion creep for the D'' region.

Anisotropic Diffusion in Postperovskite

We prepared diffusion couples of NaZnF_3 - NaXF_3 ($X = \text{Mn, Co, Fe}$) from presintered and polished pure end-member perovskite samples and annealed them at pressures ranging from ~ 2 GPa to 14 GPa and temperatures from 823 K to 1,073 K (see *SI Appendix, section S1* for details). Recovered samples were analyzed by energy-dispersive electron probe microanalysis for Zn-X concentration gradient, and a Boltzmann-Matano analysis was applied to the observed diffusion profiles. The zinc diffusivities extrapolated to pure NaZnF_3 composition (equivalent to zinc self-diffusivity) are presented in Fig. 1. The perovskite diffusion coefficients at 10 GPa and below are well fitted by the Arrhenius relation.

$$D = D_0 e^{-\frac{\Delta H + P\Delta V}{RT}}, \quad [1]$$

with parameters $\ln D_0 = 13.4 \pm 9.2 \text{ cm}^2 \cdot \text{s}^{-1}$; $\Delta H = 317 \pm 74 \text{ kJ} \cdot \text{mol}^{-1}$; $\Delta V = 5.5 \pm 1.4 \text{ cm}^3$. The 14-GPa perovskite datum falls significantly above the predicted value from the Arrhenius fit; however, this sample transformed to postperovskite during the experiment, which means that its final measured diffusivity falls between that of perovskite and postperovskite. Presynthesized postperovskite has a bulk chemical diffusivity at 14 GPa substantially larger than the predicted value for perovskite at 14 GPa and with a much smaller activation enthalpy ($88 \pm 15 \text{ kJ} \cdot \text{mol}^{-1}$, based on 2 measurements; the end-member values of the Boltzmann-Matano fits to all experiments are presented in *SI Appendix, Table S1*). The increased chemical diffusivity in postperovskite

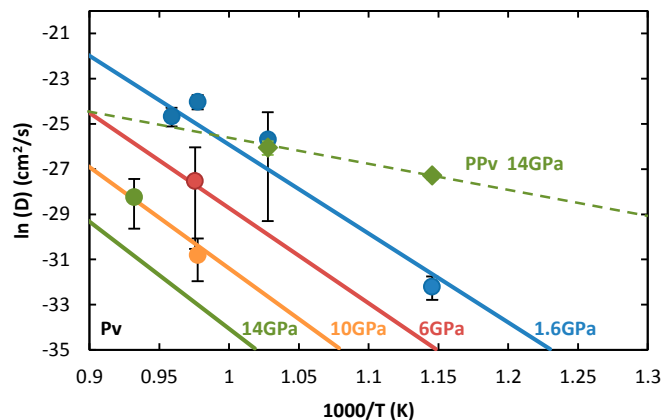


Fig. 1. Measured zinc chemical diffusivity in NaZnF_3 perovskite (circles) and postperovskite (diamonds). The Arrhenius fit to the perovskite data at pressures of 1.6 to 10 GPa are shown as solid lines, and the dashed line is the Arrhenius fit to the postperovskite diffusion data. Data are color-coded by pressure. Error bars are ± 2 SEs; the postperovskite error bars are similar to the size of the symbols.

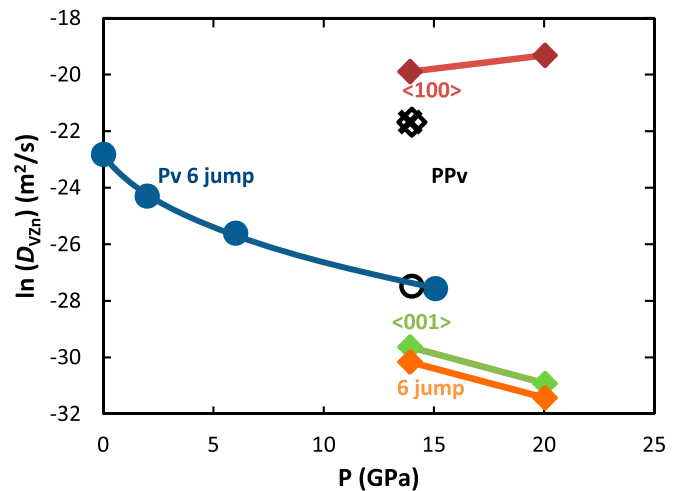


Fig. 2. Zinc vacancy diffusivity in NaZnF_3 perovskite (solid diamonds) and postperovskite (solid circles), as a function of pressure at 1,073 K, predicted from ab initio simulations. The diffusivity in perovskite is isotropic, but postperovskite shows ~ 4.5 orders of magnitude difference between the fastest $\langle 100 \rangle$ and slowest $\langle 010 \rangle$ directions. The Voigt-Reuss-Hill average of the postperovskite axial diffusivities (cross) is 2.8 orders of magnitude higher than perovskite diffusivity at 14 GPa and 1,073 K. This is in excellent agreement with the bulk diffusivity experiments (open symbols) which are plotted after conversion to vacancy diffusivities by a constant vacancy concentration of 3.5 ppm.

is also seen in the ab initio simulations of NaZnF_3 postperovskite which predict a difference in bulk Zn diffusivity between perovskite and postperovskite of 2.8 orders of magnitude at 14 GPa and 1,073 K (Fig. 2). Direct comparison of the predicted ab initio vacancy diffusivities with the experimental results requires knowledge of the vacancy concentration, which is not trivial for transition metal-bearing systems. A concentration of 3.5 parts per million (ppm) zinc vacancies per formula unit brings the experimental results into excellent agreement with the simulations for both phases. The simulated Schottky vacancy formation energies per atom at 14 GPa and resultant intrinsic Zn vacancy concentrations are, respectively, $180 \text{ kJ} \cdot \text{mol}^{-1}$ and 5 ppb for perovskite, and $170 \text{ kJ} \cdot \text{mol}^{-1}$ and 13 ppb for postperovskite. It seems reasonable, therefore, that the defect population is dominated by extrinsic vacancies under the experimental conditions. Regardless of whether the value of 3.5 ppm for the extrinsic vacancy concentration is the correct value, the ratio of zinc diffusivities in perovskite and postperovskite shows excellent agreement between the experiments and simulations.

The NaZnF_3 postperovskite simulations show a large anisotropy, with diffusion in the $\langle 100 \rangle$ direction 4.5 orders of magnitude faster than diffusion in the slowest, $\langle 010 \rangle$, direction. This sense of anisotropy is the same as that predicted for MgSiO_3 perovskite (16), and the 6-hop cycle previously found in the computer simulations to be faster than direct diffusion in the $\langle 010 \rangle$ direction also dominates here for $\langle 010 \rangle$. While the experimental measured bulk diffusivity in postperovskite agrees well with the bulk average of the predicted single-crystal values, it is necessary to compare the simulations with experimental single-crystal measurements to confirm the predicted anisotropy.

Fig. 3 shows a single crystal of NaCoF_3 postperovskite embedded in finely crystalline NaZnF_3 from a diffusion experiment at 14 GPa and 823 K. The fluoride postperovskites form with rod or needle habits (with aspect ratios ranging from 4:1 for CaIrO_3 to $>10:1$ for NaNiF_3) with their a axis parallel to the rod/needle axis (19–21). The observed diffusion profile in the direction of the long axis of the crystal is well fitted, with a codiffusivity in the single crystal of $5.3 \pm 0.42 \times 10^{-14} \text{ cm}^2/\text{s}$ and a matrix Zn

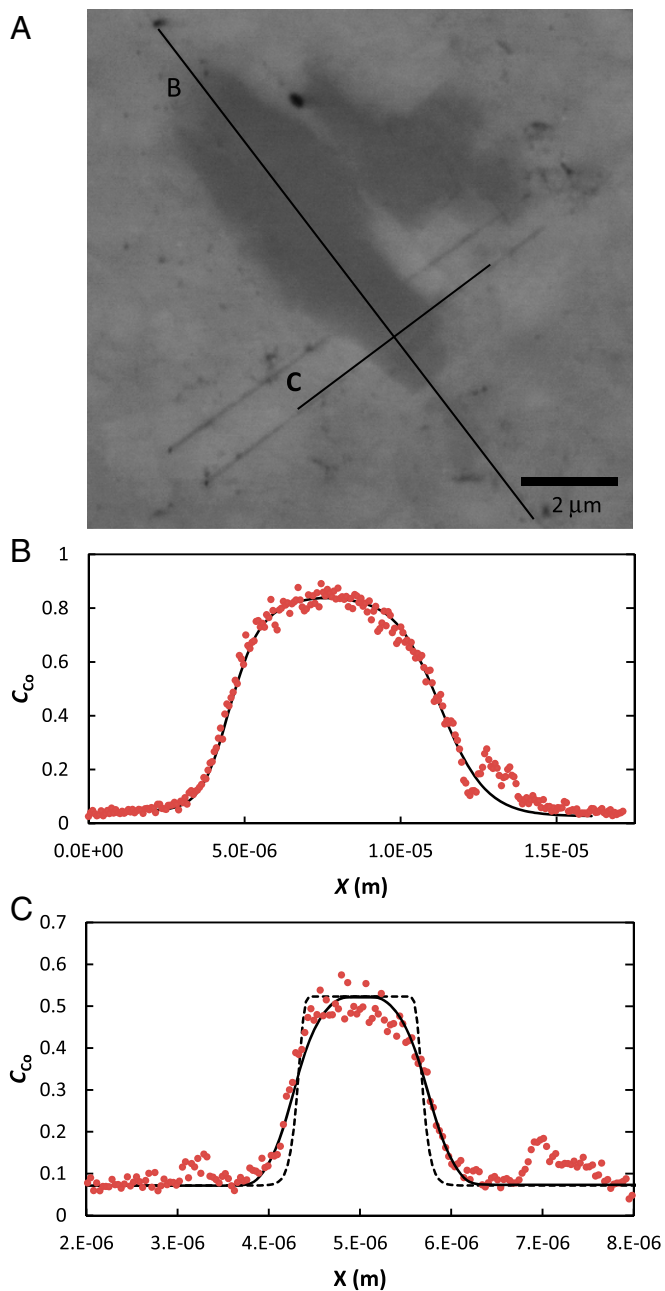


Fig. 3. Postperovskite diffusion couple of a NaCoF_3 single crystal embedded in NaZnF_3 . (A) Back-scattered electron image. (B and C) chemical analysis profile for cobalt in the (B) axial and (C) radial directions. The dashed lines are best-fitting compositionally dependent diffusion profiles, and the black lines are these profiles convolved by the analytical spot size. In the axial direction, the effect of the convolution is smaller than the width of the line.

diffusivity of $2.0 \pm 1.0 \times 10^{-14} \text{ cm}^2/\text{s}$ (Fig. 3B). The radial (i.e., perpendicular to the long axis of the crystal) diffusivity is substantially smaller, with a diffusion profile length which is similar to the analytical spot size (Fig. 3C). In this case, the beam convolution is significant to the fit—the dashed line in Fig. 3C is the best-fitting diffusion profile, and the solid line is this diffusion profile convolved with a Gaussian beam correction (22) with an SD of $0.35 \mu\text{m}$. The effect of the beam convolution in the axial direction is so small that the 2 lines are indistinguishable in Fig. 3B. The measured radial diffusivities are $6.1 \pm 3.4 \times 10^{-17} \text{ cm}^2/\text{s}$ and $7.1 \pm 2.2 \times 10^{-15} \text{ cm}^2/\text{s}$,

respectively, for the cobalt in the crystal and zinc in the matrix, giving an observed anisotropy for this crystal of 3 orders of magnitude for the single crystal but a reasonable agreement for the matrix diffusivity measured in the axial and radial directions. Multiple measurements give mean single-crystal diffusivities in the axial and radial directions of $5.5 \pm 0.3 \times 10^{-14} \text{ cm}^2/\text{s}$ and $3.7 \pm 1 \times 10^{-17} \text{ cm}^2/\text{s}$, respectively, and a Zn diffusivity of $8.2 \pm 1 \times 10^{-15} \text{ cm}^2/\text{s}$ in the matrix. We therefore observe an apparent anisotropy in NaCoF_3 postperovskite of 3 orders of magnitude at 823 K, but we consider this to be a minimum anisotropy, as our errors are likely to cause an overestimate of the diffusivity in the radial direction (SI Appendix, section S1). The inability to determine the crystal orientation in the diffusion couple, due to the small crystal size and weak metastability of fluoride postperovskite, means we are limited to comparing the axial value with the mean radial value. The long axis of postperovskite crystals is invariably the a axis in a range of systems (10, 19–21), but we cannot identify the orientation of the other 2 axes in our diffusion couple. The observed radial diffusivity displays the most variability in the experiments; if we assume that this arises from differences in the diffusivities in the b and c axial directions, then, by comparison with the simulations, we can ascribe the smallest and largest radial diffusivities to the b and c directions, respectively. This would give $D_a = 5.6 \pm 0.3 \times 10^{-14} \text{ cm}^2/\text{s}$, $D_b = 4.6 \pm 1.2 \times 10^{-18} \text{ cm}^2/\text{s}$, and $D_c = 1.7 \pm 1.3 \times 10^{-16} \text{ cm}^2/\text{s}$, or 4 orders of magnitude difference between the fastest and slowest directions, in reasonable agreement with ab initio-predicted value of 4.5 orders of magnitude. We stress here that these experiments are likely to provide minimum estimates of the anisotropy in single-crystal postperovskite diffusion.

In addition to the close agreement between experiment and simulations in the fluoride system studies, we have also found close agreement between (ab initio) predictions and experimental measurements of anisotropy in CaIrO_3 postperovskite single crystals for Pt–Ir interdiffusion (23); however, the total anisotropy in this system was only $D_a \approx 4D_b$, necessitating the present study to confirm the extreme anisotropy predicted for the silicate system. It is therefore clear that the ab initio simulations do correctly predict the anisotropy across a range of postperovskite analogs with widely varying anisotropies, as well as the absolute values for relevant systems [fluoride perovskite and postperovskite, MgSiO_3 perovskite (16), $(\text{Mg,Fe})\text{O}$ (16)] which have been measured experimentally. This sense of anisotropy can be explained by the same crystal chemical arguments as explain the more moderate anisotropy in olivine and feldspars, and the extreme values of anisotropy are largely explicable by the effect of the pressure acting on the activation volume of the diffusion in the different directions (SI Appendix, section S2). We are therefore confident that the anisotropy of chemical diffusivity from the simulations in silicate postperovskite (16), with $D_a \approx 10^4 D_c \approx 10^8 D_b$, is correct, and we now explore some consequences of extreme anisotropic chemical diffusivity for diffusion creep deformation of postperovskite in D".

Anisotropic Diffusion Creep in Postperovskite

First, we reiterate that shape anisotropy is seen in all low-pressure analog postperovskite-structured materials (19–21, 24) (and related structures such as stibnite, Sb_2S_3) and suggest that magnesium silicate postperovskite will also grow with a [100]-rod morphology. This is consistent with postperovskite morphologies which would be predicted from growth morphology theories based on lattice spacings (25–27) or attachment energies (28). Anisotropic crystal shapes result in anisotropic rheology for deformation by diffusion creep of the form $\dot{\epsilon}_i \propto D/X_i^2$, where $\dot{\epsilon}_i$ is the strain rate and X_i is the length of the crystal in the i th direction (SI Appendix, section S3). This shape-controlled creep anisotropy can be modified during the rotation of grains which is required by diffusion creep. Grain rotation during deformation

tends to break up needles and rods by microboudinage, leading to deformation-induced reduction of grain-shape anisotropy of needles (29). The processes which cause this boudinage vary depending on strain rate and temperature (30), but at least some of them can operate in the diffusion creep regime (29, 31), and can be accompanied by other processes which reduce grain size during crystal stretching in diffusion creep (31). In general, this will result in a reduction in diffusion creep strength by needle breaking and a reduction in the aspect ratio of needles, as has been seen in some industrial materials (32), but, in postperovskite, shape anisotropy does not operate in isolation, and the extreme anisotropy of chemical diffusivity must also be considered.

We derive an analytical solution for the case of rectangular grains oriented with their crystallographic axes normal to crystal faces and explore various scenarios in *SI Appendix, section S3*. Strain rates in each direction are strongly influenced by D_i/X_i^2 , where i denotes the i th direction, and X is the dimension in that direction. For anisotropies where one diffusing direction is much slower than the other 2 directions, as in postperovskite ($D_a, D_c \gg D_b$), there is no significant strain in the slow direction for any reasonable values of stress, and strain is confined to the X - Z plane. However, the relative strain rates in the other 2 directions are a complex interplay between the chemical diffusivities and crystal dimensions in those directions. The evolution of a grain

of MgSiO_3 postperovskite, with initial dimensions of $1 \text{ mm} \times 1 \text{ mm} \times 1 \text{ mm}$, under core–mantle boundary conditions and an applied differential stress of 5 MPa is presented in Fig. 4. The figure shows that it is easy to stretch equant grains parallel to the a -axial direction and shrink them in the c -axial direction, but difficult to do the stretch along c . Thus, beginning with a random crystallographic preferred orientation (CPO), we predict the preferential development of bladed needles with the long axis parallel to a . Strain rates for extension parallel to X , parallel to the fast diffusing axial direction, are up to 500 times higher than for shortening parallel to X . Extension parallel to X also produces strain weakening by a factor of 50 after the first ~ 50 Ma, while shortening just induces gradual strengthening. Both these observations are a consequence of the strain being initially rate limited by D_c/Z^2 ; for stretching along X , the crystal is shrinking in the Z dimension, whereas, for compressions along X , Z must increase to conserve volume. However, once X is sufficiently large, the strain becomes rate-limited by D_a/X^2 , and, with continued strain, the strain rate decreases. Taken at face value, this would suggest that the strain weakening is transient, but, as discussed above, large shape anisotropies tend to be unstable against shear, with boudinage processes limiting the aspect ratio of grains. The maximum strain rate for the scenario shown in Fig. 4 occurs when $X = 11 \text{ mm}$, $Y = 1 \text{ mm}$, and $Z = 90 \mu\text{m}$ which, with an aspect ratio of over 100:1, will be susceptible to boudinage and hence grain size (and aspect ratio) reduction. We therefore suggest that ongoing deformation will result in continued strain weakening by stretching along X accompanied by repeated boudinage.

Deformation in D''

We have shown that the extreme anisotropy of diffusivity in postperovskite should result in strain-weakening rheology. In addition to strain weakening, the formation of bladed needles of the form shown in Fig. 4 will result in development of a shape-preferred orientation, since anisotropic grains undergoing shear settle with their long axes parallel to elongation and their intermediate axes perpendicular to the shear profile plane as shown in numerical models of anisotropic ellipsoids under shear strain (*SI Appendix, sections S4 and S5*). Since the shape anisotropy is a result of diffusion anisotropy, this also implies CPO formation with a axes oriented parallel to the stretching direction and b axes oriented perpendicular to the shear profile plane. There are several experimental studies which show that the generation of CPO is possible during diffusion creep deformation of olivine (33, 34) and anorthite (35). Here we show that, in addition to those examples of texture generation in diffusion creep, anisotropic chemical diffusivity should, in itself, generate texture by formation of strongly anisotropic crystal shapes. Development of CPO in mica has been observed in micaceous metapelites accompanied by preferential diffusion creep along the fast diffusion direction [in that case, diffusion within the mica (001) plane is ~ 4 orders of magnitude faster than diffusion perpendicular to this plane] (36). For MgSiO_3 postperovskite, deforming by diffusion creep in a horizontal flow field along the core–mantle boundary texture will develop with a axes oriented parallel to the flow direction with c axes oriented vertically.

As dislocation creep is generally thought to be a requirement to produce CPO, the observation of seismic anisotropy in D'' has led to the common assumption that dislocation creep must dominate deformation in D''. However, our results show that anisotropic diffusion creep in postperovskite is also able to produce CPO, and, as discussed earlier, diffusion creep is, in fact, more consistent with the strain rates and stress expected in the D'' region (37) and the likely grain size of postperovskite (*SI Appendix, section S6*). An anisotropic diffusion creep controlled deformation mechanism of the form described here has a number of fundamental

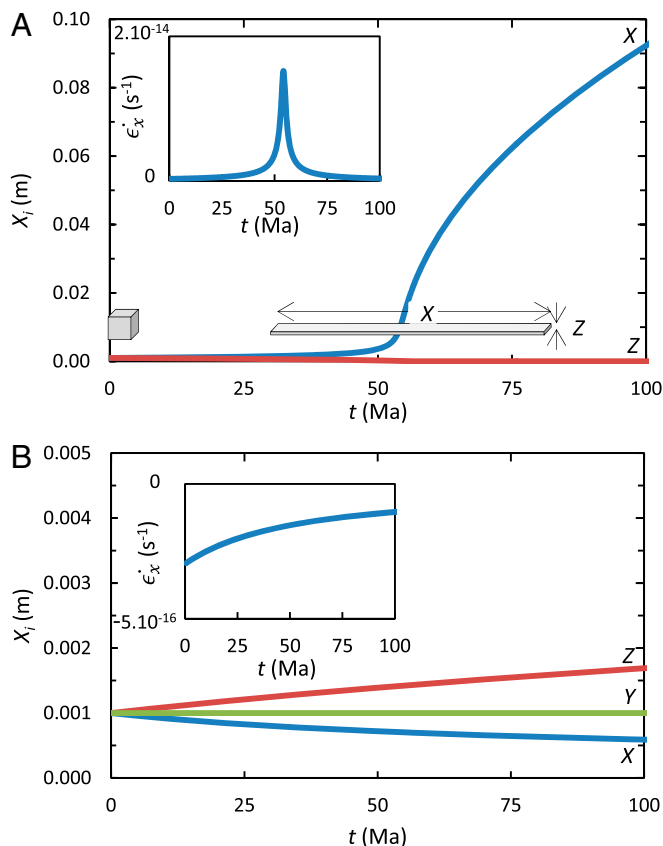


Fig. 4. Time evolution of grain dimensions for an initially cubic crystal of MgSiO_3 postperovskite of volume 1 mm^3 under a differential stress of 5 MPa for (A) tension parallel to a and (B) tension parallel to c . The axial diffusivities are $D_a = 10^{-16} \text{ m}^2/\text{s}$, $D_b = 10^{-22} \text{ m}^2/\text{s}$, and $D_c = 10^{-20} \text{ m}^2/\text{s}$, consistent with ref. 16 at 120 GPa and 4,000 K and a vacancy concentration of 10^{-5} . The crystal axial lengths, X , Y , and Z , are parallel to crystallographic axes a , b , and c , and *Insets* show strain rates parallel to X for situations in A and B (the strain rate in Y is near zero, and that in Z is equal, but opposite, to that in X). The length evolution of Y , being negligible, is omitted. Starting crystal shape and shape at maximum strain rate are sketched in A.

implications for the Earth's lowermost mantle. The first is that postperovskite will be much weaker than perovskite, even when cooler. This is because postperovskite deforming by diffusion creep will be controlled predominantly by the fastest diffusing direction. This is also consistent with recent atomistic simulations which show that postperovskite deforming by dislocation creep will also be weak (13), so, regardless of which deformation mechanism is operating, this finding is robust. Weak postperovskite means that cool subducting slabs in D'' will be weaker than warmer perovskite-bearing LLSVP regions, making LLSVPs more resistant to being deformed or pushed about by slabs. Secondly, the anisotropy formed by diffusion creep will not have the same dependence on strain as dislocation creep, and so mapping mantle flow from anisotropy with diffusion creep will produce a different flow pattern than flow models previously based on dislocation creep. The third implication is that postperovskite deforming by diffusion creep in D'' will exhibit a strain-weakening rheology. Strain weakening results in localization of deformation onto shear zones (38). This is observed on all length scales in both brittle and plastic deformation, and is a key to generating plate tectonic-style convection in Earth (38). We suggest that a similar process might operate in the D'' region, resulting in strain being localized in narrow shear zones of strongly textured postperovskite with larger regions between these shear zones suffering relatively little deformation. This will allow previously developed textures to survive in the nondeforming regions, something that would be very

problematic when mapping seismic anisotropy onto mantle flow. Also, rapid changes in observed seismic wave speed (39) which are currently interpreted as compositional variations might simply be due to adjacent regions of very different anisotropy brought into close proximity along shear zones. In addition, shear zones which display a substantially different seismic anisotropy from their surroundings might contribute to scattering in the lowermost mantle. The development of shear zones within postperovskite-dominated regions might also contribute to the long-term survival of the large low shear velocity regions by localization of strain to their outermost margins. Strong localization of strain may also have a strong effect on heat flow in D'' , due to the anisotropic thermal conductivity of postperovskite (40, 41). If, as we argue, postperovskite dominated regions of D'' are, in fact, deforming by diffusion creep, texture generation and strain localization are likely to exert strong controls on the dynamics of D'' . These processes should therefore be considered in future geodynamical and seismic studies of this region.

Data Availability Statement

All data are available in the main text or *SI Appendix*.

ACKNOWLEDGMENTS. This work was funded by Natural Environment Research Council Grants NE/L006898 and NE/L007363, and a Friedrich Wilhelm Bessel Research Award of the Alexander von Humboldt Stiftung to D.P.D. We thank Florian Heidelbach for assistance with SEM analyses.

- M. Murakami, K. Hirose, K. Kawamura, N. Sata, Y. Ohishi, Post-perovskite phase transition in MgSiO_3 . *Science* **304**, 855–858 (2004).
- A. R. Oganov, S. Ono, Theoretical and experimental evidence for a post-perovskite phase of MgSiO_3 in Earth's D'' layer. *Nature* **430**, 445–448 (2004).
- T. Tsuchiya, J. Tsuchiya, K. Umamoto, R. M. Wentzcovitch, Phase transition in MgSiO_3 perovskite in the Earth's lower mantle. *Earth Planet. Sci. Lett.* **224**, 241–248 (2004).
- J. Wookey, J. M. Kendall, Constraints on lowermost mantle mineralogy and fabric beneath Siberia from seismic anisotropy. *Earth Planet. Sci. Lett.* **275**, 32–42 (2008).
- S. Merkel *et al.*, Deformation of $(\text{Mg,Fe})\text{SiO}_3$ post-perovskite and D'' anisotropy. *Science* **316**, 1729–1732 (2007).
- A. M. Walker, A. M. Forte, J. Wookey, A. Nowacki, J.-M. Kendall, Elastic anisotropy of D'' predicted from global models of mantle flow. *Geochem. Geophys. Geosyst.* **12**, Q10006 (2011).
- H.-R. Wenk, S. Cottaar, C. N. Tomé, A. McNamara, B. Romanowicz, Deformation in the lowermost mantle: From polycrystal plasticity to seismic anisotropy. *Earth Planet. Sci. Lett.* **306**, 33–45 (2011).
- L. Miyagi, W. Kanitpanyacharoen, P. Kaercher, K. K. M. Lee, H.-R. Wenk, Slip systems in MgSiO_3 post-perovskite: Implications for D'' anisotropy. *Science* **329**, 1639–1641 (2010).
- S. Merkel *et al.*, Plastic deformation of MgGeO_3 post-perovskite at lower mantle pressures. *Science* **311**, 644–646 (2006).
- R. J. McCormack, D. P. Dobson, N. Walte, N. Miyajima, T. Taniguchi, The development of shape- and crystallographic-preferred orientation in CaPtO_3 post-perovskite deformed in pure shear. *Am. Mineral.* **96**, 1630–1636 (2011).
- D. P. Dobson *et al.*, Inherited textures during the perovskite to post-perovskite transition and seismic anisotropy in D'' . *Nat. Geosci.* **6**, 575–578 (2013).
- S. A. Hunt *et al.*, Weakening of CaIrO_3 during the perovskite-post perovskite transformation. *Nat. Geosci.* **2**, 794–797 (2009).
- A. M. Goryaeva, P. Carrez, P. Cordier, Modeling defects and plasticity in MgSiO_3 post-perovskite: Part 3—Screw and edge $[001]$ dislocations. *Phys. Chem. Miner.* **44**, 521–533 (2017).
- A. R. Walker, D. P. Dobson, J. Wookey, A. Nowacki, A. Forte, The anisotropic signal of topotaxy during phase transitions in D'' . *Phys. Earth Planet. Inter.* **276**, 159–171 (2018).
- S. A. Hunt, A. M. Walker, E. Mariani, In-situ measurement of fabric development rate in CaIrO_3 . *Phys. Earth Planet. Inter.* **259**, 91–104 (2016).
- M. W. Ammann, J. P. Brodholt, J. Wookey, D. P. Dobson, First-principles constraints on diffusion in lower-mantle minerals and a weak D'' layer. *Nature* **465**, 462–465 (2010).
- S.-i. Karato, The influence of anisotropic diffusion on the high-temperature creep of a polycrystalline aggregate. *Phys. Earth Planet. Inter.* **183**, 468–472 (2010).
- T. Yoshino, D. Yamazaki, Grain growth kinetics of CaIrO_3 perovskite and post-perovskite, with implications for rheology of D'' layer. *Earth Planet. Sci. Lett.* **255**, 485–493 (2007).
- D. P. Dobson, S. A. Hunt, A. Lindsay-Scott, I. G. Wood, Towards better analogues for MgSiO_3 post-perovskite: NaCoF_3 and NaNiF_3 , two new recoverable post-perovskite phases. *Phys. Earth Planet. Inter.* **189**, 171–175 (2011).
- A. Lindsay-Scott *et al.*, Time-of-flight neutron powder diffraction with milligram samples: The crystal structures of NaCoF_3 and NaNiF_3 post-perovskites. *J. Appl. Crystal.* **47**, 1939–1947 (2014).
- A. Lindsay-Scott, "The thermoelastic properties of post-perovskite analogue phases," PhD thesis, University of London, London, United Kingdom (2012).
- D. P. Dobson, R. W. Thomas, T. M. Mitchell, Diffusion profiles around quartz clasts as indicators of the thermal history of pseudotachylytes. *Geochem. Geophys. Geosyst.* **19**, 4329–4341 (2018).
- R. J. McCormack, "The rheological and transport properties of deep-mantle materials," PhD thesis, University of London, London, United Kingdom (2012).
- Y. Shirako *et al.*, High-pressure stability relations, crystal structures, and physical properties of perovskite and post-perovskite of NaNiF_3 . *J. Solid State Chem.* **191**, 167–174 (2012).
- A. Bravais, *Études Crystallographiques* (Gauthier Villars, Paris, France, 1866).
- J. Donnay, D. Harker, A new law of crystal morphology extending the law of Bravais. *Am. Mineral.* **22**, 446–467 (1937).
- M. Friedel, Etudes sur la loi de Bravais. *Bull. Soc. Française Mineral.* **30**, 326–455 (1907).
- P. Hartman, P. Bennema, The attachment energy as a habit controlling factor: I. Theoretical considerations. *J. Cryst. Growth* **49**, 145–156 (1980).
- B. Perumal, M. A. Rist, S. Gungor, J. W. Brooks, M. E. Fitzpatrick, The effect of hot deformation parameters on microstructure evolution of the α -phase in Ti-6Al-4V. *Metall. Material. Trans. A* **47**, 4128–4136 (2016).
- I. Sen, R. S. Kottada, U. Ramamurty, High temperature processing maps for boron modified Ti-6Al-4V alloys. *Mater. Sci. Eng. A* **527**, 6157–6165 (2010).
- D. Elliott, Diffusion flow laws in metamorphic rocks. *Geol. Soc. Am. Bull.* **84**, 2645–2664 (1973).
- S. Y. Yoon, T. Akatsu, E. Yasuda, Anisotropy of creep deformation rate in hot-pressed Si_3N_4 with preferred orientation of the elongated grains. *J. Mater. Sci.* **32**, 3813–3819 (1997).
- T. Miyazaki, K. Sueyoshi, T. Hiraga, Olivine crystals align during diffusion creep of Earth's upper mantle. *Nature* **502**, 321–326 (2013).
- M. Sundberg, R. F. Cooper, Crystallographic preferred orientation produced by diffusional creep of harzburgite: Effects of chemical interactions among phases during plastic flow. *J. Geophys. Res.* **113**, B12208 (2008).
- J. Gómez Barreiro *et al.*, Preferred orientation of anorthite deformed experimentally in Newtonian creep. *Earth Planet. Sci. Lett.* **264**, 188–207 (2007).
- N. S. Mancktelow, The development of slaty cleavage. *Tectonophysics* **58**, 1–20 (1979).
- A. K. McNamara, P. E. van Keken, S. Karato, Development of anisotropic structure in the Earth's lower mantle by solid-state convection. *Nature* **416**, 310–314 (2002).
- F. Gueydan, J. Précigout, L. G. J. Montési, Strain weakening enables continental plate tectonics. *Tectonophysics* **631**, 189–196 (2014).
- Y. Wang, L. Wen, Mapping the geometry and geographic distribution of a very low velocity province at the base of the Earth's mantle. *J. Geophys. Res.* **109**, B10305 (2004).
- S. A. Hunt *et al.*, On the increase in thermal diffusivity caused by the perovskite to post-perovskite phase transition and its implications for mantle dynamics. *Earth Planet. Sci. Lett.* **319**, 96–103 (2012).
- M. W. Ammann *et al.*, Variation of thermal conductivity and heat flux at the Earth's core mantle boundary. *Earth Planet. Sci. Lett.* **390**, 175–185 (2014).